

1           **Distributions of Tropical Precipitation Cluster Power and Their**  
2           **Changes Under Global Warming. Part I: observational baseline and**  
3           **comparison to a high-resolution atmospheric model**

4

5                                   KEVIN M. QUINN and J. DAVID NEELIN

6

7           *Department of Atmospheric and Oceanic Sciences, University of California, Los Angeles,*  
8                                   *Los Angeles, California*

9

10          *Corresponding author address:* Kevin M. Quinn, Department of Atmospheric and  
11          Oceanic Sciences, UCLA, 7127 Math Science Building, 405 Hilgard Avenue, Los  
12          Angeles, CA 90095-1565. E-mail: kquinn@atmos.ucla.edu

13

14

15                                   **ABSTRACT**

16           The total amount of precipitation integrated across a precipitation feature  
17          (contiguous precipitating grid cells exceeding a minimum rain rate) is a useful measure of  
18          the aggregate size of the disturbance, expressed as the rate of water mass lost or latent  
19          heat released, i.e. the power of the disturbance. The probability distribution of cluster

20 power is examined over the Tropics using Tropical Rainfall Measuring Mission (TRMM)  
21 3B42 satellite-retrieved rain rates and global climate model output. Observed  
22 distributions are scale-free from the smallest clusters up to a cutoff scale at high cluster  
23 power, after which the probability drops rapidly. After establishing an observational  
24 baseline, precipitation from the High Resolution Atmospheric Model (HIRAM) at two  
25 horizontal grid spacings (roughly 0.5 and 0.25°) are compared. When low rain rates are  
26 excluded by choosing a minimum rain rate threshold in defining clusters, the model  
27 accurately reproduces observed cluster power statistics at both resolutions. Middle and  
28 end-of-century cluster power distributions are investigated in HIRAM in simulations with  
29 prescribed sea surface temperatures and greenhouse gas concentrations from a “business  
30 as usual” global warming scenario. The probability of high cluster power events increases  
31 strongly by end-of-century, exceeding a factor of 10 for the highest power events for  
32 which statistics can be computed. Clausius-Clapeyron scaling accounts for only a fraction  
33 of the increased probability of high cluster power events.

34

34

35 1. Introduction

36 Extremes of precipitation intensity are projected to change across all global  
37 warming scenarios in the Coupled Model Intercomparison Project Phase 3 (CMIP3) and  
38 CMIP5 experiments (Tebaldi et al. 2006; Kharin et al. 2007, 2013; O’Gorman and  
39 Schneider 2009; Sillmann et al. 2013a,b). Tebaldi et al. (2006) review historical and  
40 future simulations from a suite of 9 coupled global climate models across multiple  
41 emissions scenarios, finding a clear signal of increased precipitation intensity emerging  
42 by end-of-century over the globe. Kharin et al. (2007 and 2013) also analyze a suite of  
43 coupled climate models for consistency in projections of extreme precipitation spanning  
44 the CMIP3 and CMIP5 experiments, finding shorter wait times for extreme precipitation  
45 events by end-of-century relative to historical climate, and that the intensity of extreme  
46 precipitation events increases at a rate of 6% per ° C of warming across both CMIP3 and  
47 CMIP5 experiments. Additionally, Sillmann et al. (2013b) find that several metrics of  
48 precipitation extremes increase proportional to warming.

49 Uncertainties regarding changes in precipitation extremes emerge in both  
50 observations (e.g., Easterling et al. 2000; Alexander et al. 2006; Kharin et al. 2007, 2013;  
51 Lenderink and van Meijgaard 2008; Allan et al. 2010) and in global-scale simulations of  
52 extreme precipitation in recent climate and future climate (e.g., Tebaldi et al. 2006;  
53 Kharin et al. 2007, 2013; Allan and Soden 2008; Allan et al. 2010; Sillmann et al.  
54 2013a,b). Kharin et al. (2007) hypothesize that, over the Tropics, uncertainty in simulated  
55 extreme precipitation results from limitations in the representation of associated physical  
56 processes in climate models. Additionally, simulated precipitation extremes from an

57 ensemble of 19 CMIP3 models are lower than observed precipitation extremes from  
58 1987-2004 (Allan and Soden 2008). Chen and Knutson (2008) note that when  
59 considering extreme precipitation events, modeled precipitation should be analyzed as  
60 areal averages versus point estimates. At regional scales, a survey of climate model  
61 studies using multiple approaches (e.g., multi-model ensembles, downscaling) suggests  
62 that projected changes to extreme precipitation event frequency and intensity also exhibit  
63 large regional variability (e.g., Beniston et al. 2007; Kay and Washington 2008;  
64 Seneviratne et al. 2012; Vizzy and Cook 2012; Haensler et al. 2013; Stocker et al. 2013;  
65 Barros et al. 2014; Sylla et al. 2015).

66 Characterizing changes in the frequency and intensity of organized convection,  
67 including in tropical cyclones, is important because of their potential socio-economic  
68 impacts. Many studies into tropical cyclone changes under global warming suggest that  
69 overall global tropical cyclone frequency will decrease by end-of-century (e.g., Emanuel  
70 et al. 2008; Knutson et al. 2008, 2010, 2013; Bender et al. 2010), though tropical cyclone  
71 intensity is projected to increase, both measured by higher rain rates and hurricane  
72 category (e.g., Webster et al. 2005; Emanuel et al. 2008; Gualdi et al. 2008; Knutson et al.  
73 2008, 2013; Bender et al. 2010). Changes in tropical cyclone intensity under global  
74 warming are further investigated in climate model simulations by Knutson et al. (2013),  
75 Villarini et al. (2014), and Wehner et al. (2015). Decreases in the total number of tropical  
76 cyclones but increases in intense tropical cyclones in future climate under global  
77 warming are described in Knutson et al. (2013) and Wehner et al. (2015). Rainfall rates  
78 associated with tropical cyclones are projected to increase (Knutson et al. 2013; Villarini  
79 et al. 2014; Wehner et al. 2015), scaling with the Clausius-Clapeyron (CC) relationship in

80 some regions (Knutson et al. 2013; Villarini et al. 2014), but exceeding results expected  
81 under CC-scaling near centers of tropical cyclones (Knutson et al. 2013; Wehner et al.  
82 2015). More generally, changes in convective organization, as noted in observations by  
83 Tan et al. (2015), may be important to changes in precipitation extremes.

84 Work to better understand processes of convective organization (e.g., Leary and  
85 Houze 1979; Houze 1982; Houze 1989; Mapes and Houze 1993; Houze 2004) in current  
86 climate includes studies of the self-aggregation of tropical convection over smaller  
87 domains (e.g., Bretherton et al. 2005; Muller and Held 2012; Khairoutdinov and Emanuel  
88 2013; Wing and Emanuel 2014; Wing and Cronin 2015). The aggregation of convection  
89 into clusters has been shown to be sensitive to: hydrometeor parameterization (Bretherton  
90 et al. 2005); Coriolis forcing (Bretherton et al. 2005); low cloud distribution (Muller and  
91 Held 2012); SST changes (Khairoutdinov and Emanuel 2013); and advection of moist  
92 static energy (Wing and Cronin 2015). Additionally, Wing and Emanuel (2014) note that  
93 processes that initiate the aggregation of convective cells into clusters (e.g., atmospheric  
94 water vapor absorbing shortwave radiation, surface heat flux) are different than processes  
95 that maintain aggregation once it has already occurred (e.g., longwave radiation  
96 feedback). Cluster aggregation processes at smaller scales appear to continue into  
97 idealized large domains in modeling studies (Holloway et al. 2012; Bretherton and  
98 Khairoutdinov 2015; Arnold and Randall 2015).

99 Observational studies of tropical precipitation clusters over large domains include  
100 Mapes et al. (2009), Peters et al. (2009, 2010, 2012), Wood and Field (2011), and Skok et  
101 al. (2013). In Skok et al. (2013), space-time clusters are defined to analyze precipitation  
102 statistics associated with tropical cyclones, using satellite-retrieved precipitation

103 estimates from the Tropical Rainfall Measuring Mission (TRMM-3B42). Mapes et al.  
104 (2009) examines cluster lifecycle and size distributions using IR and scatterometer data  
105 sets over the Tropics, noting that small clusters with brief lifespans constitute the vast  
106 majority of oceanic storm clusters. Wood and Field (2011) and Peters et al. (2009, 2010,  
107 2012) analyze storm cluster organization using a variety of observational datasets, noting  
108 that probability distributions of cluster cloud area (Peters et al. 2009; Wood and Field  
109 2011), precipitation integrated across contiguous precipitating clusters (cluster power,  
110 Peters et al. 2012) or precipitation accumulations, i.e. precipitation integrated across  
111 temporal events (Peters et al. 2010) follow a long, scale-free power law, with a distinct  
112 cutoff, i.e. a more rapid drop in frequency of occurrence, at large cluster area and high  
113 power. Cluster power behavior above the cutoff is different than behavior below the  
114 cutoff, in part because different physical processes drive daily tropical convection and  
115 tropical cyclones (Peters et al. 2012). Furthermore, Peters et al. (2012) noted that tropical  
116 cyclones provide significant contributions to the tail in the large event regime. Neelin et  
117 al. (2017) find changes in end-of-century precipitation accumulations, especially for  
118 changes in probability of the very largest accumulations. This is associated with the form  
119 of the distribution, and in particular with the physics that determines how the cutoff scale  
120 changes with warming, motivating examination here of analogous behavior for spatial  
121 clusters.

122         There is a need for the validation of rainfall simulations in climate models,  
123 especially extreme events in quantities likely important for changes under global  
124 warming, such as measures of organized convection. Distributions of precipitation  
125 integrated across a cluster over the Tropics are thus examined here for the first time as i)

126 a potentially useful measure both as a metric of model simulation in current climate and ii)  
127 as a measure of changes in tropical disturbances in simulations of future climate. This  
128 integrated precipitation can be described as cluster power (defined here as the  
129 instantaneous latent heat release integrated over a cluster of contiguous precipitating grid  
130 cells). Distributions and tail sensitivity to the most powerful storm clusters at a global  
131 scale are examined in satellite observations with full spatial coverage and compared to  
132 climate model simulations for the first time, examining the relationship between cluster  
133 power and rain rate across a global domain. We first establish an observational baseline  
134 using satellite-retrieved precipitation data to test its usefulness for comparison to climate  
135 model output at two resolutions. Second, we assess how reliably a high resolution climate  
136 model can simulate historical cluster power distributions. Lastly, we apply output from  
137 future runs of the same model to examine mid- and end-of-century simulated cluster  
138 power distributions, quantifying the influence of global warming on cluster power  
139 behavior. These results for a high-resolution model set the stage for further examination  
140 of lower resolution coupled models from the CMIP5 archive in Part II.

141

## 142 2. Data and Methods

143 Satellite-retrieved rain rate data from the Tropical Rainfall Measuring Mission  
144 (TRMM-3B42) program are used to build a baseline of cluster power behavior. Data  
145 from sensors onboard the TRMM spacecraft are merged with data from other satellites to  
146 provide gap-free TRMM-3B42 rain rate data over oceans and land, and are available  
147 beginning in 1998 (Huffman et al. 2007; TRMM 2015). These data have units of  
148 millimeters per hour and are available every three hours over a  $0.25^{\circ} \times 0.25^{\circ}$  latitude-

149 longitude grid. For consistency with our comparisons in Part II, we analyze twice daily  
150 TRMM-3B42 time slices at 00 UTC and 12 UTC. To calculate cluster power,  
151 precipitating grid cells meeting a minimum rain rate threshold are first aggregated into  
152 distinct clusters. From there, cluster power is expressed as the instantaneous latent heat  
153 release integrated over a cluster in units of gigawatts by multiplying rain rates by the  
154 latent heat of condensation ( $2.5 \times 10^6 \text{ J kg}^{-1}$ ), which relates cluster power to the Earth's  
155 energy budget. Cluster power can also be expressed equivalently in terms of a mass  
156 budget as the integrated mass of water lost per hour ( $\text{kg H}_2\text{O hr}^{-1}$ ) with 1 GW equal to  
157  $1.4 \times 10^6 \text{ kg H}_2\text{O hr}^{-1}$  lost.

158         Precipitation data from the Geophysical Fluid Dynamics Laboratory (GFDL)  
159 High Resolution Atmospheric Model (HIRAM) at two horizontal resolutions are  
160 incorporated into this study: HIRAM-C360 (25 km) and HIRAM-C180 (50 km) (Zhao et  
161 al. 2009, 2010; Chen and Lin 2011; Held and Zhao 2011; Zhao and Held 2011, 2012;  
162 Merlis et al. 2013; Villarini et al. 2014; GFDL 2015). HIRAM output is derived from the  
163 historical Atmospheric Model Intercomparison Project (AMIP, 1979-2008) and future  
164 (SST2030, 2026-2035 and SST2090, 2086-2095) experiments, incorporating prescribed  
165 sea surface temperatures (SSTs) from the Met Office Hadley Centre Sea Ice and SST  
166 version 1.1 model (Rayner et al. 2003) for the historical period, and greenhouse gas and  
167 SST anomalies from the GFDL-Earth System Model 2 (ESM2) for future runs.  
168 Precipitation data are given at three hourly intervals in units of precipitation flux ( $\text{kg m}^{-2}$   
169  $\text{s}^{-1}$ ), though to stay consistent with the TRMM-3B42 retrieval, instantaneous HIRAM  
170 cluster power snapshots from only 00 UTC and 12 UTC with rain rates meeting a  
171 minimum threshold are aggregated into distinct clusters. These clusters then have their

172 rate of water mass loss converted to instantaneous latent heat release, using the same  
173 method as the TRMM-3B42 dataset. Next, we compare AMIP simulation output with  
174 satellite-retrieved data to assess its accuracy in simulating historical conditions. After  
175 establishing an accurate AMIP baseline, we then use these AMIP simulations for the  
176 comparison with future climate simulations, with C360 data directly compared to  
177 observed data due to their comparable spatial resolution.

178         The binning procedure in building probability density functions (PDFs) for these  
179 distributions is as follows. One wants to have bin width increase smoothly as  
180 probabilities drop, for which a bin width that is approximately constant in log space is  
181 suitable. It is important also to recognize that the increments of cluster size are quantized  
182 to multiples of the minimum cluster size. To ensure that the bin spacing is consistent with  
183 this, bin widths are adjusted to the integer multiple of the minimum cluster size that is  
184 closest to the asymptotic constant bin width chosen for the upper end of the distribution.  
185 In practice, the variations in bin are small; Table 1 of the Supplementary Information  
186 shows both bin width and histogram counts  $N_i$  prior to normalization by the width of bin  $i$   
187 and the total counts for each analysis presented. Error bars are given by  $\pm N_i^{1/2}$ , with the  
188 same normalization as the PDF. The minimum cluster size is set by the grid size and the  
189 minimum precipitation threshold, so the same bin boundaries apply to historical and  
190 future climate runs of the same dataset. Cluster power distributions for 1 May-30  
191 September are shown over a global tropics domain from 30<sup>0</sup>S to 30<sup>0</sup>N. To illustrate the  
192 extent to which cluster power behavior is influenced by domain size a northern Atlantic-  
193 East Pacific domain, extending from the Equator to 30<sup>0</sup>N and from 140<sup>0</sup>W across the

194 Americas and Atlantic Ocean to  $0^{\circ}\text{E}$ , is shown in the Supplementary Information. Cluster  
195 power distributions were also examined over other domains yielding similar results.

196

### 197 3. Analysis

#### 198 3.1 Cluster Power Distributions: Observations

199 Previous cluster studies have analyzed cluster quantities such as cloud area above  
200 a certain reflectivity threshold (Wood and Field 2011), storm cluster area and duration  
201 using IR imagery and scatterometer data (Mapes et al. 2009), and cluster area and power  
202 using satellite radar and passive microwave imagery (Peters et al. 2009, 2012). In the  
203 case of radar imagery, these have been for narrow swaths, limited by the radar swath  
204 width. In Figure 1 we form an observational baseline for cluster power using satellite-  
205 retrieved rain rate data, evaluating the merged satellite TRMM-3B42 retrieval at a global  
206 scale over land and ocean, so statistics are not limited by swath width. Figure 1 examines  
207 TRMM-3B42 cluster power distributions for multiple rain rate thresholds at a global  
208 scale.

209 Across the Tropics at multiple rain rate thresholds (Figure 1), TRMM-3B42  
210 cluster power distributions follow a long, scale-free power law, similar to Peters et al.  
211 (2012), which noted an exponent of -1.87 in the TRMM radar 2A25 retrieval. The  
212 exponent here (as estimated from the slope of the least squares best-fit line over the  
213 power law range at the  $0.7 \text{ mm hr}^{-1}$  rain rate threshold in Fig. 1) is -1.50. In Fig. 1, the  
214 cutoff that terminates the power law range for all rain rate thresholds lies at  
215 approximately  $10^5 \text{ GW}$ , with the frequency of the highest power clusters for all

216 distributions falling off more rapidly after the cutoff. This cutoff also appears to be  
217 insensitive to rain rate threshold. Note that the cluster power of the lowest power bin  
218 depends on rain rate threshold, simply because the minimum cluster power is a function  
219 of the minimum rain rate considered and the grid cell size. Cluster power distributions  
220 must begin at a threshold-dependent minimum power and are shifted slightly because this  
221 affects the normalization of the probability distribution.

222         To provide further context for this distribution, Figure S1 shows the distribution  
223 of cluster area (previously examined in other data sets by Mapes and Houze 1993; Peters  
224 et al. 2009), which likewise exhibits an approximate power law range followed by a  
225 reduction in probability above the cutoff scale. The cutoff scale for area is more  
226 dependent on rain rate threshold than that for power in the total rate of water loss from  
227 the cluster is a physically important quantity, so we focus on cluster power. To provide a  
228 sense of how whether the cluster power distribution might change if evaluated over a  
229 particular subset of the tropics, Figure S2 shows comparable results for the Atlantic-East  
230 Pacific region. The power law range has similar exponent (-1.42 versus -1.50) and the  
231 cutoff occurs at a similar power.

232         Intriguingly, the form of the cluster power probability distribution is similar to  
233 what occurs for temporal clusters, i.e. accumulations of precipitation over events, in a  
234 simple prototype model (Stechmann and Neelin 2011, 2014; Neelin et al. 2017) that also  
235 exhibits a power law range with approximately exponential cut off. The exponent of that  
236 simple configuration, -1.5, is close to the exponent for precipitation integrated over  
237 spatial clusters here. An apparent exponent of -1.2 or steeper, depending on convective  
238 parameters, was noted for the power law range in cluster area distributions in a similar

239 simple model (Hottovy and Stechmann 2015), but no quantitative prototype appears to  
240 exist yet for integrated cluster precipitation. For continuity with previous literature,  
241 probability distributions for cluster area are shown for reference in Fig. 1 of the  
242 Supplementary Information (SI). Similar to the power distributions, an approximately  
243 power-law range is found for cluster area, extending from the minimum area ( $7 \times 10^8 \text{ m}^2$ )  
244 to a qualitatively similar cutoff at around  $3 \times 10^{11} \text{ m}^2$ , with exponent of approximately -1.7.  
245 The cutoff for area distributions exhibits slightly more dependence on rain rate threshold.  
246 We choose the integrated precipitation/power for the cluster for the remainder of this  
247 work because of its greater physical importance due to the correspondence to total water  
248 loss/latent heat release from the cluster.

249 Figure 2 displays typical satellite-retrieved cluster morphology at the lowest and  
250 highest minimum rain rate thresholds considered in this study ( $0.1 \text{ mm hr}^{-1}$  and  $0.7 \text{ mm}$   
251  $\text{hr}^{-1}$ ) for a sample day in 2004. Most clusters at the  $0.1 \text{ mm hr}^{-1}$  rain rate threshold with  
252 high cluster power ( $\geq 10^5 \text{ GW}$ ) resemble tropical cyclones, mesoscale convective systems,  
253 ITCZ-like features, or the tail ends of mid-latitude fronts that occasionally pass between  
254  $20^\circ$  and  $30^\circ \text{N/S}$ . At the  $0.7 \text{ mm hr}^{-1}$  rain rate threshold, overall structure of most features  
255 remains the same, with only some trimming on the edges of the largest features. These  
256 examples of cluster morphology are provided simply to illustrate the phenomena that are  
257 being condensed into the distributions, and provide a sense of why little variation in  
258 cluster power behavior across rain rate thresholds occurs in the observational  
259 distributions.

260

261 3.2. Cluster Power Distributions: Historical HIRAM Output

262 Figures 3-5 quantify how the HIRAM at two horizontal resolutions approximates  
263 observed cluster power behavior. Figure 3 compares HIRAM cluster power distributions  
264 at multiple rain rate thresholds, while Figure 4 displays HIRAM distributions at two  
265 resolutions. Figure 5 overlays HIRAM-C360 and TRMM-3B42 cluster power  
266 distributions at two rain rate thresholds.

267 Like the TRMM-3B42 dataset (Figure 1), HIRAM cluster power distributions  
268 (Figures 3-4) are also scale-free along a power law range, have a cutoff around  $10^5$  GW,  
269 and display little sensitivity to rain rate threshold along the power law range before the  
270 cutoff. Additionally, HIRAM distribution least squares best-fit exponents (for the 0.7 mm  
271  $\text{hr}^{-1}$  threshold) range from -1.36 to -1.39 (depending on horizontal resolution), similar to  
272 the TRMM-3B42 analysis (-1.50, Figure 1). The lower resolution simulation (C180) has  
273 a shorter scale-free region due to coarser resolution resulting in a larger minimum cluster  
274 area and hence larger minimum cluster power. The C180 PDF is slightly further from the  
275 observations in the sense that probability density drops slightly less steeply than that of  
276 C360. Otherwise, its scale-free power law range and cutoff closely parallel that from the  
277 higher resolution simulation (Figure 4).

278 Tail behavior sensitivity to rain rate threshold is quantified in Figure 3. While  
279 TRMM-3B42 distributions exhibit little sensitivity, HIRAM distributions do exhibit  
280 substantial sensitivity above the cutoff for low rain rate thresholds. At rain rate thresholds  
281 below  $0.3 \text{ mm hr}^{-1}$ , the cutoff shifts towards higher power. This finding is consistent with  
282 previous findings that global climate models can overestimate light precipitation

283 coverage (e.g., Dai 2006). Beginning at a rain rate threshold of  $0.3 \text{ mm hr}^{-1}$  and above,  
284 tails of the distributions converge, suggesting that it is important to exclude low rain rates  
285 from clusters and that higher minimum rain rate thresholds are more robust for  
286 comparison with observations. For an illustration of the spatial behavior of modeled  
287 precipitation clusters, refer to Figures S3-S4 in the SI.

288         The comparison between TRMM-3B42 and HIRAM-C360 cluster power  
289 distributions in Figure 6 shows that, in general, the tail of the modeled power distribution  
290 at the  $0.7 \text{ mm hr}^{-1}$  rain rate threshold more closely parallels the TRMM-3B42 distribution.  
291 Although their least squares best-fit exponents are slightly different ( $-1.39$  for HIRAM-  
292 C360, Figure 3,  $-1.50$  for TRMM-3B42, Figure 1), and the tail of the TRMM-3B42  
293 distribution is longer, the tails for both distributions at high power are very similar.

294         We also ask how HIRAM-C360 cluster power distributions compare to  
295 distributions from a synthetic time series created from the same data that deliberately  
296 removes any spatial relations beyond those that would occur from the climatological  
297 probability of precipitation (Figure 5). Clusters can occur even in simple systems in  
298 which there is no spatial correlation and under certain circumstances these can have  
299 power law distributions (Stauffer and Aharony, 1994; for discussion in a meteorological  
300 context see, e.g., Peters et al. 2009) —due diligence thus requires that we verify that the  
301 reproduction of observed cluster distributions by HIRAM is well distinguished from such  
302 a simple case. The synthetic time series is analogous to a statistical null hypothesis model,  
303 in that strong differences between HIRAM-C360 cluster power distributions and those of  
304 the synthetic time series provide evidence that spatial relations simulated dynamically in  
305 the model are key to producing the pdf. To build the synthetic time series that preserves

306 rain rate probabilities while artificially removing these spatial relations, we select rain  
307 rate values for each grid cell from random time steps at the same spatial location using  
308 HIRAM-C360 data from 1 May-30 September 1979-1999. The rain rate probabilities as a  
309 function of space are preserved, but all other spatial autocorrelation effects are destroyed.  
310 Clusters are then evaluated from the synthetic time series at rain rate thresholds of 0.3  
311  $\text{mm hr}^{-1}$  and  $0.7 \text{ mm hr}^{-1}$  just as for the actual HIRAM-C360 output, and the PDFs are  
312 compared. The synthetic time series distributions clearly have different structures than  
313 the observed/HIRAM distributions; the power law range, if present, is too short to be  
314 clearly seen, and distinct cutoffs occur at relatively low cluster power. This comparison  
315 suggests that the features of the observed cluster PDF captured by HIRAM are not  
316 obtained just by chance occurrence of neighboring raining points.

317

### 318 3.3. Cluster Power Distributions: Future HIRAM Output

319 Changes in the frequency of high cluster power events (e.g., tropical cyclones)  
320 may have large societal repercussions. As a result, we examine changes in future cluster  
321 power distributions (Figures 6-7) by comparing historical (AMIP), mid-century  
322 (SST2030), and end-of-century (SST2090) cluster power distributions at the  $0.7 \text{ mm hr}^{-1}$   
323 rain rate threshold used in this study. Historical, mid-century, and end-of-century  
324 distributions are very similar to each other before the cutoff, following the same long,  
325 scale-free power law range (Figure 6). By end-of-century, there is a clear signal in both  
326 simulations that indicates a shift towards higher power in the tail region, implying more  
327 frequent intense storm clusters (Figure 6). This increase (for the highest three bins for

328 which statistics can be calculated, which span a factor of 4 in storm power —  $2 \times 10^5$  GW  
329 to  $8 \times 10^5$  GW) is a factor of approximately 3, 10, and almost 20, respectively, as  
330 indicated on Figure 7a for the highest resolution simulation by end-of-century. Figure 7b  
331 shows an alternate means of displaying this information as a form of risk ratio (Otto et al.  
332 2012), specifically, showing the ratio of the probability density. This increases rapidly  
333 for the largest cluster sizes, similar to time-domain results for accumulations (Neelin et al.  
334 2017) which exhibited an approximately exponential increase for the largest  
335 accumulations. The end of century also has events of unprecedented size, as may be seen  
336 in Fig. 7a, but these are not shown in Fig. 7b since they would be estimated as infinite  
337 ratio. Figure 7b also shows a test of robustness of the binning procedure, showing two  
338 cases with slightly smaller asymptotic bin widths, for which the last bin with nonzero  
339 counts in the historical period is shifted by approximately half a bin width and almost one  
340 bin width, respectively. These yield highly consistent results over the portion of the curve  
341 that they estimate. Additionally, if instead of considering changes to the probabilities of  
342 fixed bins, we consider how the tail of the distribution *extends*, the probability  
343 corresponding to the highest power bin in the historical period shifts to higher power —  
344 for the end-of-century this probability occurs for a power that has increased by roughly a  
345 factor of 1.4 relative to current climate (Figure 7a).

346 Other studies (e.g., Knutson et al. 2013; Villarini et al. 2014; Wehner et al. 2015)  
347 have compared changes in modeled rain rates under global warming scenarios with  
348 changes expected under Clausius-Clapeyron (CC) scaling of humidity, so to test a  
349 possible physical explanation for the increased probability of intense storm clusters by  
350 end-of-century, we examine changes to cluster power distributions under a realistic

351 global warming scenario. The difference in mean global temperature between HIRAM-  
352 C360 SST2090 and AMIP experiments is +2.16 K, within the range of temperature  
353 increase projected by Stocker et al. (2013). Assuming a 7% increase in specific humidity  
354 per 1 K warming under the CC relationship, this represents a possible 15.12% increase in  
355 precipitation under global warming. Given this warming, we multiply HIRAM-C360  
356 AMIP rain rates (at the 0.7 mm hr<sup>-1</sup> threshold) by a factor of 1.15, re-cluster (keeping the  
357 same threshold), and then re-analyze this CC-scaled dataset, comparing its distribution of  
358 cluster power to HIRAM-C360 AMIP and SST2090 distributions.

359         The application of a CC-scaling factor to the HIRAM-C360 AMIP dataset does  
360 increase frequency of the most powerful storm clusters and shift the tail region of the CC-  
361 scaled dataset towards higher power compared to the original HIRAM-C360 AMIP  
362 dataset (Figure 7c). However, this application appears to only account for a fraction of  
363 the increased probability of the most intense storm clusters, suggesting that the increased  
364 probability of the most intense storm clusters by end-of-century is significantly higher  
365 than that expected based on a simple CC-scaling of precipitation intensity. Knutson et al.  
366 (2013) and Wehner et al. (2015) also found that rain rate increases surrounding the cores  
367 (e.g., within 200 km) of intense tropical cyclones under global warming exceed rain rate  
368 increases that would be expected solely under CC scaling of precipitation, hypothesizing  
369 a link between this exceedance and the dynamics driving the intensity around the cores of  
370 intense tropical cyclones. Wang et al (2015) also note a link between an increase in  
371 precipitation rates near storm centers, CC-scaling, and the dynamics affecting the  
372 convergence near storm centers. In a different study, Knutson et al (2015) find that where  
373 end-of-century SST increases are particularly large, though not uniform globally, the

374 amount of precipitation associated with intense hurricanes also increases at a rate  
375 exceeding CC-scaling of precipitation. Although detailed analysis of spatial structures  
376 beyond the scope of this work, Fig. S4 provides examples of storms from the large-power  
377 end of the distribution for reference.

378

#### 379 **4. Summary and Discussion**

380 Observed cluster power distributions are found to follow a long, scale-free power  
381 law between  $10 - 10^5$  GW, with a rapid drop off in the frequency of storm clusters with  
382 high cluster power thereafter. In units of mass loss, the cutoff near  $10^5$  GW is equivalent  
383 to approximately  $10^{11}$  kg hr<sup>-1</sup>. The phenomena leading to these clusters range from  
384 convective phenomena at the grid cell scale (approximately 25 km) and mesoscale  
385 clusters through ITCZ disturbances and tropical cyclones. The cutoff at high power is  
386 largely independent of rain rate in the observations, and here is found in a data set not  
387 limited by swath width, or land versus ocean retrievals. This suggests that some set of  
388 physical factors within the tropical climate system and the meteorology of storm  
389 aggregation must lead to the existence of the cutoff, as further discussed below.

390 HIRAM simulations at both resolutions for the historical period accurately  
391 reproduce observed distributions using a minimum rain rate threshold of  $0.7$  mm hr<sup>-1</sup>,  
392 with similar least squares best-fit exponents over the power law range (-1.5 for TRMM-  
393 3B42, -1.39/-1.36 for HIRAM-C360/C180). At both model resolutions, the cutoff at high  
394 power is correctly produced near  $10^5$  GW, suggesting that model resolution has little  
395 impact on simulating cluster power. HIRAM cutoff values are sensitive to rain rate

396 threshold, due to overly widespread occurrence of low rain rates, but agree well provided  
397 the threshold is not too low.

398         A first step in posing the question of what processes might be important to this  
399 distribution shape is to ask whether the HIRAM simulation of the atmospheric dynamics  
400 driving the aggregation of neighboring contiguous precipitating grid cells can be  
401 distinguished from simpler processes that might be hypothesized to account for some of  
402 the effects. The simplest process that can create clusters potentially exhibiting such a  
403 distribution, including a power law range under certain circumstances, would be one in  
404 which precipitation occurs with observed probabilities but without the dynamical  
405 information of spatial relations. Constructing a synthetic time series from the HIRAM-  
406 C360 data but with the spatial relation between grid cells destroyed by randomizing the  
407 time step from which the rain rate sample is drawn provides a simple foil that acts like a  
408 null hypothesis. The cluster power distributions resulting from the synthetic time series  
409 are quantitatively well distinguished from the observed and HIRAM distributions. This  
410 verifies that the atmospheric dynamics driving cluster distributions in HIRAM are more  
411 complex than simply yielding reasonable probabilities of precipitation.

412         The long scale-free range in both observations and HIRAM but not in the simplest  
413 case tested by the synthetic time series suggests that the length and slope of the scale-free  
414 range, as well as the apparent change of dynamical regimes at the cutoff, constitute  
415 interesting targets for explanation in modeling of cluster aggregation. Theory has recently  
416 been developed for the distribution of precipitation accumulation—the integral of  
417 precipitation over the time for which it exceeds a specified threshold — which is the  
418 analog in the time domain of the cluster power integrated over spatially continuous points.

419 The accumulation distribution with a power law range followed by a roughly exponential  
420 cut off seen in observations (Peters et al. 2010) and models (Neelin et al. 2017) can be  
421 mimicked by stochastic models for the prognostic column moisture equation (Stechmann  
422 and Neelin 2014; Neelin et al. 2017). In the time domain case, fluctuations of moisture  
423 convergence drive variations of moisture, with the time derivative of moisture providing  
424 a memory of previous states. Precipitation accumulation corresponds to the physical  
425 effect of the integrated loss of moisture. The cutoff scale is set by the interplay between  
426 the magnitude of the moisture convergence fluctuations and the integrated loss and thus  
427 increases under global warming as moisture convergence fluctuations increase (Neelin et  
428 al. 2017). Creating analogous theory for the spatial case is desirable but is a nontrivial  
429 undertaking, given the complex processes creating horizontal relations between  
430 neighboring columns, including moisture transport by convergent and rotational  
431 components of the flow, gravity wave dynamics, and radiative interactions. We  
432 conjecture that model experiments in idealized domains or with interventions in model  
433 dynamics that have been used to study various aspects of aggregation (e.g., Bretherton et  
434 al. 2005; Muller and Held 2012; Holloway et al. 2012; Khairoutdinov and Emanuel 2013;  
435 Wing and Emanuel 2014; Wing and Cronin 2015; Bretherton and Khairoutdinov 2015;  
436 Arnold and Randall 2015) might feasibly be used to determine if the cutoff scale found  
437 here corresponds to any fundamental physical scale of the system.

438           Because the cutoff affects the probability of the highest cluster power events,  
439 potentially very important for human impacts, changes to cluster power distributions  
440 under global warming are examined. HIRAM cluster power distributions at both  
441 resolutions from the future SST2030 and SST2090 experiments have the same long,

442 scale-free range as historical HIRAM output, but the cutoff tends to shift toward higher  
443 power. A natural simple hypothesis to compare against for the increased probability of  
444 more intense storms by end-of-century, is a CC-scaling of the precipitation to factor in  
445 the simplest impacts of temperature on specific humidity. Specifically, a CC-scaling  
446 factor of 7% increase per degree of warming under the projected change to mean global  
447 temperature (2.16 K, calculated using HIRAM-C360 AMIP and SST2090 temperature  
448 data) was applied to the HIRAM-C360 AMIP dataset before running the same clustering  
449 and binning procedures. The resulting cluster power distribution with this hypothetical  
450 CC-scaled precipitation lies between the original AMIP and SST2090 cluster power  
451 distributions, indicating that the change in future cluster power distributions considerably  
452 exceeds expectations based on a simple CC-scaling of rain rates.

453         The shift of the cutoff toward higher cluster power in the warmer climate has a  
454 substantial impact on the frequency of occurrence of the largest storms. The probability  
455 of high cluster power events for the end of century relative to the historical period  
456 increases rapidly beyond the historical cutoff. These increases substantially exceed a  
457 factor of 10 for the highest bin for which cluster power statistics can be computed in the  
458 historical period. Phrased another way, at the corresponding value of probability for the  
459 highest bin in which statistics can be computed for the historical period, the end of  
460 century clusters would be roughly 40% more powerful.

461

462 *Acknowledgments*

463

464 This project was supported in part by the National Science Foundation (NSF Grant AGS-  
465 1540518) and National Oceanic and Atmospheric Administration (NOAA Grants  
466 NA14OAR4310274 and NA15OAR4310097). Portions of this material have been  
467 presented at the 96<sup>th</sup> Annual Meeting of the American Meteorological Society in 2016.  
468 We thank the National Aeronautics and Space Administration (NASA) and Japan  
469 Aerospace Exploration Agency (JAXA) for producing their observational precipitation  
470 data sets, available at  
471 [http://disc.sci.gsfc.nasa.gov/datacollection/TRMM\\_3B42\\_daily\\_V7.html](http://disc.sci.gsfc.nasa.gov/datacollection/TRMM_3B42_daily_V7.html). Additionally,  
472 we would like to acknowledge the NOAA/Geophysical Fluid Dynamics Laboratory  
473 (GFDL) for producing their model output, available at  
474 <http://nomads.gfdl.noaa.gov:8080/DataPortal/cmip5.jsp>. We thank N. Berg, K. Hales-  
475 Garcia, M. Schwartz, and D. Walton for assistance in procedure development and J.  
476 Meyerson for graphics support.

477

478 **References:**

479 Alexander, L. V., and Coauthors, 2006: Global observed changes in daily extremes of  
480 temperature and precipitation. *J. Geophys. Res. Atmos.*, **111**, D05109, doi:  
481 10.1029/2005JD006290.

482 Allan, R. P., and B. J. Soden, 2008: Atmospheric warming and the amplification of  
483 precipitation extremes. *Science*, **321**, 1481-1484.

484 ———, B. J. Soden, V. O. John, W. Ingram, and P. Good, 2010: Current changes in  
485 tropical precipitation. *Environ. Res. Lett.*, **5**, 1-7, doi:10.1088/1748-9326/5/2/025205.

486 Arnold, N. P., and D. A. Randall, 2015: Global-scale convective aggregation:  
487 Implications for the Madden-Julian Oscillation. *J. Adv. Model. Earth Syst.*, **7**, 1499-1518,  
488 doi:10.1002/2015MS000498

489 Barros, V. R., and Coauthors, 2014: IPCC, 2014: *Climate Change 2014: Impacts,*  
490 *Adaptation, and Vulnerability. Part B: Regional Aspects. Contribution of Working*  
491 *Group II to the Fifth Assessment Report of the Intergovernmental Panel on Climate*  
492 *Change*. Cambridge University Press, 688 pp.

493 Bender, M. A., T. R. Knutson, R. E. Tuleya, J. J. Sirutis, G. A. Vecchi, S. T. Garner, and  
494 I. M. Held, 2010: Modeled impact of anthropogenic warming on the frequency of intense  
495 Atlantic hurricanes. *Science*, **327**, 454–458.

496 Beniston, M., and Coauthors, 2007: Future extreme events in European climate: an  
497 exploration of regional climate model projections. *Climatic Change*, **81(1)**, 71-95.

498 Bretherton, C. S., P. N. Blossey, and M. Khairoutdinov, 2005: An energy-balance  
499 analysis of deep convective self-aggregation above uniform SST. *J. Atmos. Sci.*, **62**,  
500 4273-4292.

501 ———, and M. Khairoutdinov, 2015: Convective self-aggregation feedbacks in near-global  
502 cloud-resolving simulations of an aquaplanet. *J. Adv. Model. Earth Syst.*, **7**, 1765-1787,  
503 doi: 10.1002/2015MS000499

504 Chen, C.-T., and T. Knutson, 2008: On the verification and comparison of extreme  
505 rainfall indices from climate models. *J. Climate*, **21**, 1605–1621,  
506 doi:[10.1175/2007JCLI1494.1](https://doi.org/10.1175/2007JCLI1494.1).

507 Chen, J. H., and S. J. Lin, 2011: The remarkable predictability of inter-annual variability  
508 of Atlantic hurricanes during the past decade. *Geophys. Res. Lett.*, **38**, L11804,  
509 doi:10.1029/2011GL047629.

510 Dai, A., 2006: Precipitation characteristics in eighteen coupled climate models. *J.*  
511 *Climate*, **19**, 4605-4630, doi:10.1175/JCLI3884.1.

512 Easterling, D. R., G. A. Meehl, C. Parmesan, S. A. Chagnon, T. R. Karl, and L. O.  
513 Mearns, 2000: Climate extremes: Observations, modeling, and impacts. *Science*, **289**,  
514 2068-2074, doi: 10.1126/science.289.5487.2068.

515 Emanuel, K. A., R. Sundararajan, and J. Williams, 2008: Hurricanes and global warming:  
516 Results from downscaling IPCC AR4 simulations. *Bull. Amer. Meteor. Soc.*, **89**, 347–367.

517 Geophysical Fluid Dynamics Laboratory (GFDL), 2015: Global atmospheric models.  
518 Accessed 30 November 2015. [Available online at  
519 <http://www.gfdl.noaa.gov/atmospheric-model>.]

520 Gualdi, S., E. Soccimarro, and A. Navarra, 2008: Changes in tropical cyclone activity due  
521 to global warming: Results from a high-resolution coupled general circulation model. *J.*  
522 *Climate*, **21**, 5204–5228.

523 Haensler, A., F. Saeed, D. Jacob, 2013: Assessing the robustness of projected  
524 precipitation changes over central Africa on the basis of a multitude of global and  
525 regional climate projections. *Climatic Change*, **121(2)**, 349-363.

526 Held, I. M. and M. Zhao, 2011: The response of tropical cyclone statistics to an increase  
527 in CO<sub>2</sub> with fixed sea surface temperatures. *J. Climate*, **24**, 5353-5364,  
528 doi:10.1175/JCLI-D-11-00050.1.

529 Holloway, C. E., S. J. Woolnough, and G. M. Lister, 2012: Precipitation distributions for  
530 explicit versus parametrized convection in a large-domain high-resolution tropical case  
531 study. *Quart. J. Roy. Meteor. Soc.*, **138**, 1692–1708, doi:10.1002/qj.1903.

532 Hottovy, S., and S. N. Stechmann, 2015: A spatiotemporal stochastic model for tropical  
533 precipitation and water vapor dynamics. *J. Atmos. Sci.*, **72**, 4721-4738, doi:10.1175/JAS-  
534 D-15-0119.1.

535 Houze, R. A., 1982: Cloud clusters and large-scale vertical motions in the tropics. *J.*  
536 *Meteorol. Soc. Japan*, **60(1)**, 396-410.

537 ———, 1989: Observed structure of mesoscale convective systems and implications for  
538 large-scale heating. *Quart. J. Roy. Meteor. Soc.*, **115**, 425-461.

539 ———, 2004: Mesoscale convective systems, *Rev. Geophys.*, **42**, RG4003,  
540 doi:10.1029/2004RG000150.

541 Huffman, G. J., and Coauthors, 2007: The TRMM multisatellite precipitation analysis  
542 (TMPA): Quasi-global, multiyear, combined-sensor precipitation estimates at fine  
543 scales. *J. Hydrometeor.*, **8**, 38–55, doi:10.1175/JHM560.1.

544 Kay, G., and R. Washington, 2008: Future southern African summer rainfall variability  
545 related to a southwest Indian Ocean dipole in HadCM3. *Geophys. Res. Lett.*, **35**, L12701,  
546 doi: 10.1029/2008GL034180.

547 Kharioutdinov, M., and K. A. Emanuel, 2013: Rotating radiative-convective equilibrium  
548 simulated by a cloud-resolving model. *J. Adv. Model. Earth Syst.*, **5**, 816–825, doi:  
549 10.1002/2013MS000253

550 Kharin, V. V., F. W. Zwiers, X. Zhang, and G. C. Hegerl, 2007: Changes in temperature  
551 and precipitation extremes in the IPCC Ensemble of Global Coupled Model  
552 Simulations. *J. Climate*, **20**, 1419–1444, doi:10.1175/JCLI4066.1.

553 ———, and M. F. Wehner, 2013: Changes in temperature and precipitation extremes in the  
554 CMIP5 ensemble. *Climatic Change*, **119.2**, 345–357, doi:10.1007/s10584-013-0705-8.

555 Knutson, T. R., J. J. Sirutis, S. T. Garner, G. A. Vecchi, and I. M. Held, 2008: Simulated  
556 reduction in Atlantic hurricane frequency under twenty-first-century warming conditions.  
557 *Nat. Geosci.*, **1**, 359–364.

558 ———, and Coauthors, 2010: Tropical cyclones and climate change. *Nat. Geosci.*, **3**, 157–  
559 163.

560 ———, and Coauthors, 2013: Dynamical downscaling projections of twenty-first-century  
561 Atlantic hurricane activity: CMIP3 and CMIP5 model-based scenarios. *J. Climate*, **26(17)**,  
562 6591–6617, doi:10.1175/JCLI-D-12-00539.1.

563 ———, R., J. Sirutis, M. Zhao, R. Tuleya, M. Bender, G. Vecchi, G. Villarini,  
564 and D. Chavas, 2015: Global projections of intense tropical cyclone activity for the late  
565 twenty-first century from dynamical downscaling of CMIP5/RCP4.5 scenarios. *J.*  
566 *Climate*, **28**, 7203–7224, doi:[10.1175/JCLI-D-15-0129.1](https://doi.org/10.1175/JCLI-D-15-0129.1).

567 Leary, C. A., and R. A. Houze, 1979: The structure and evolution of convection in a  
568 tropical cloud cluster. *J. Atmos. Sci.*, **36**, 437–457, doi:10.1175/1520-  
569 0469(1979)036<0437:TSAEOC>2.0.CO;2.

570 Lenderink, G., and E. Van Meijgaard, 2008: Increase in hourly precipitation extremes  
571 beyond expectations from temperature changes. *Nature Geosci.*, **1(8)**, 511-514.

572 Mapes, B., and R. A. Houze, 1993: Cloud clusters and superclusters over the oceanic  
573 warm pool. *Mon. Wea. Rev.*, **121**, 1398-1415.

574 ———, R. Milliff, and J. Morzel, 2009: Composite life cycle of maritime tropical  
575 mesoscale convective systems in scatterometer and microwave satellite observations. *J.*  
576 *Atmos. Sci.*, **66**, 199–208, doi:10.1175/2008JAS2746.1.

577 Merlis, T. M., M. Zhao, and I. M. Held, 2013: The sensitivity of hurricane frequency to  
578 ITCZ changes and radiatively forced warming in aquaplanet simulations. *Geophys. Res.*  
579 *Lett.*, **40**, 4109-4114, doi:10.1002/grl.50680.

580 Muller, C. J., and I. M. Held, 2012: Detailed Investigation of the self-aggregation of  
581 convection in cloud-resolving simulations. *J. Atmos. Sci.*, **69**, 2551–2565,  
582 doi:10.1175/JAS-D-11-0257.1.

583 Neelin, J. D., S. Sahany, S. N. Stechmann, and D. Bernstein, 2017: Global warming  
584 precipitation accumulation increases above the current-climate cutoff scale. *Proc. Natl.*  
585 *Acad. Sci. USA*, **114**, 6 1258–6 1263.

586 O’Gorman, P. A., and T. Schneider, 2009: The physical basis for increases in  
587 precipitation extremes in simulations of twenty-first-century climate change. *Proc. Natl.*  
588 *Acad. Sci. USA*, **106**, 14 773–14 777.

589 Otto FEL, Massey N, van Oldenborgh GJ, Jones RG, Allen MR (2012) Reconciling  
590 two approaches to attribution of the 2010 Russian heat wave. *Geophys Res Lett*  
591 39(4):L04702.

592 Peters, O., J. D. Neelin, and S. W. Nesbitt, 2009: Mesoscale convective systems and  
593 critical clusters. *J. Atmos. Sci.*, **66.9**, 2913-2924, doi:10.1175/2008JAS2761.1.

594 —, A. DeLuca, A. Corral, J. D. Neelin, and C. E. Holloway, 2010: Universality of rain  
595 event size distributions. *Journal of Statistical Mechanics: Theory and Experiment*, **11**, 1-  
596 15, doi:10.1088/1742-5468/2010/11/P11030\_

597 —, K. Christensen, and J. D. Neelin, 2012: Rainfall and Dragon-Kings. *The European*  
598 *Physical Journal Special Topics*, **205.1**, 147-158, doi:10.1140/epjst/e2012-01567-5.

599 Rayner, N. A., D. E. Parker, E. B. Horton, C. K. Folland, L. V. Alexander, D. P.  
600 Rowell, E. C. Kent, and A. Kaplan, 2003: Global analyses of sea surface temperature, sea  
601 ice, and night marine air temperature since the late nineteenth century. *J. Geophys.*  
602 *Res.*, **108**, 4407, doi:[10.1029/2002JD002670](https://doi.org/10.1029/2002JD002670).

603 Seneviratne, S.I., and Coauthors, 2012: Changes in climate extremes and their impacts on  
604 the natural physical environment. *Managing the risks of extreme events and disasters to*  
605 *advance climate change adaptation*. Cambridge University Press, 121 pp.

606 Sillmann, J., V. V. Kharin, X. Zhang, F. W. Zwiers, and D. Bronaugh, 2013a: Climate  
607 extremes indices in the CMIP5 multimodel ensemble: Part 1. Model evaluation in the  
608 present climate. *J. Geophys. Res. Atmos.*, **118**, 1716-1733, doi:10.1002/jgrd.50203.

609 —, 2013b: Climate extremes indices in the CMIP5 multimodel ensemble: Part 2.  
610 Future climate projections. *J. Geophys. Res. Atmos.*, **118**, 2473–2493,  
611 doi:10.1002/jgrd.50188.

612 Skok, G., J. Bacmeister, and J. Tribbia, 2013: Analysis of tropical cyclone precipitation  
613 using an object-based algorithm. *J. Climate*, **26**, 2563–2579, doi:10.1175/JCLI-D-12-  
614 00135.1.

615 Stauffer, D., and A. Aharony, 1994: *Introduction to Percolation Theory*. 2nd ed. Taylor  
616 and Francis, 181 pp.

617 Stechmann, S. N., and J. D. Neelin, 2011: A stochastic model for the transition to strong  
618 convection. *J. Atmos. Sci.*, **68**, 2955–2970, doi:10.1175/JAS-D-11-028.1.

619 —, 2014: First-passage-time prototypes for precipitation statistics. *J. Atmos. Sci.*, **71**,  
620 3269–3291, doi:10.1175/JAS-D-13-0268.1.

621 Stocker, T. F., and Coauthors, 2013: *Climate Change 2013: The Physical Science Basis*.  
622 *Contribution of Working Group I to the Fifth Assessment Report of the Intergovernmental*  
623 *Panel on Climate Change*. Cambridge University Press, 1535 pp.

624 Sylla, M. B., F. Giorgi, J. S. Pal, P. Gibba, I. Kebe, and M. Nikiema, 2015: Projected  
625 changes in the annual cycle of high-intensity precipitation events over west Africa for the  
626 late twenty-first century. *J. Climate*, **28**, 6475–6488, doi:10.1175/JCLI-D-14-00854.1.

627 Tan, J., C. Jakob, W. B. Rossow, and G. Tselioudis, 2015: Increases in tropical rainfall  
628 driven by changes in frequency of organized deep convection. *Nature*, **519**, 451–460,  
629 doi:10.1038/nature14339.

630 Tebaldi C., K. Hayhoe, J. M. Arblaster, and G. A. Meehl, 2006: Going to the extremes:  
631 An intercomparison of model-simulated historical and future changes in extreme events.  
632 *Climate Change*, **79**, 185–211. doi:10.1007/s10584-006-9051-4.

633 Tropical Rainfall Measuring Mission Project (TRMM), 2015: Daily TRMM and Others  
634 Rainfall Estimate (3B42 V7 derived), version 7. Goddard Space Flight Center Distributed  
635 Active Archive Center (GSFC DAAC). Accessed 01 July 2015. [Available online at  
636 [http://disc.sci.gsfc.nasa.gov/datacollection/TRMM\\_3B42\\_daily\\_V7.html](http://disc.sci.gsfc.nasa.gov/datacollection/TRMM_3B42_daily_V7.html).]

637 Villarini, G., D. Lavers, E. Scoccimarro, M. Zhao, M. Wehner, G. Vecchi, T. Knutson,  
638 and K. Reed, 2014: Sensitivity of tropical cyclone rainfall to idealized global scale  
639 forcings. *J. Climate*, **27**, 4622–41, doi:10.1175/JCLI-D-13-00780.1.

640 Vizzy, E. K., and K. H. Cook, 2012: Mid-twenty-first-century changes in extreme events  
641 over northern and tropical Africa. *J. Climate*, **25**, 5748–5767, doi:10.1175/JCLI-D-11-  
642 00693.1.

643 Wang, C.-C., B.-X. Lin, C.-T. Chen, and S.-H. Lo, 2015: Quantifying the effects of long-  
644 term climate change on tropical cyclone rainfall using a cloud-resolving model:  
645 Examples of two landfall typhoons in Taiwan. *J. Climate*, **28**, 66–85, doi:[10.1175/JCLI-](https://doi.org/10.1175/JCLI-D-14-00044.1)  
646 [D-14-00044.1](https://doi.org/10.1175/JCLI-D-14-00044.1).

647 Webster, P. J., G. J. Holland, J. A. Curry, and H.-R. Chang, 2005: Changes in tropical  
648 cyclone number, duration, and intensity in a warming environment. *Science*, **309**, 1844–  
649 1846.

650 Wehner, M., M. Prabhat, K. A. Reed, D. Stone, W. D. Collins, and J. Bacmeister, 2015:  
651 Resolution dependence of future tropical cyclone projections of CAM5.1 in the U.S.

652 CLIVAR hurricane working group idealized configurations. *J. Climate*, **28**, 3905-3925,  
653 doi: 10.1175/JCLI-D-14-00311.1.

654 Wing, A. A., and K. A. Emanuel, 2014: Physical mechanisms controlling self-  
655 aggregation of convection in idealized numerical modeling simulations. *J. Adv. Model.*  
656 *Earth Syst.*, **6**, 59–74, doi:10.1002/2013MS000269.

657 ———, and T. W. Cronin, 2015: Self-aggregation of convection in long channel geometry.  
658 *Quart. J. Roy. Meteor. Soc.*, **142**, 1-15, doi:10.1002/qj.2628.

659 Wood, R., and P. R. Field, 2011: The distribution of cloud horizontal sizes. *J. Climate*, **24**,  
660 4800-4816, doi:10.1175/2011JCLI4056.1.

661 Zhao, M., I. M. Held, S. J. Lin, and G. A. Vecchi, 2009: Simulations of global hurricane  
662 climatology, interannual variability, and response to global warming using a 50-km  
663 resolution GCM. *J. Climate*, **22**, 6653-6678, doi:10.1175/2009JCLI3049.1.

664 ———, I. M. Held, and G. A. Vecchi, 2010: Retrospective forecasts of the hurricane season  
665 using a global atmospheric model assuming persistence of SST anomalies. *Mon. Wea.*  
666 *Rev.*, **138**, 3858-3868, doi:10.1175/2010MWR3366.1.

667 ———, and I. M. Held, 2011: An analysis of the effect of global warming on the intensity  
668 of Atlantic hurricanes using a GCM with statistical refinement. *J. Climate*, **23**, 6382-6393,  
669 doi:10.1175/2010JCLI3837.1.

670 ———, 2012: TC-permitting GCM simulations of hurricane frequency response to sea  
671 surface temperature anomalies projected for the late-twenty-first-century. *J. Climate*, **25**,  
672 2995-3009, doi: 10.1175/JCLI-D-11-00313.1.

673

674 **Figure captions:**

675 Fig. 1 Probability distributions of cluster power, i.e., precipitation integrated over clusters of  
676 contiguous pixels exceeding the specified rain rate threshold, expressed in units of latent heat  
677 release (gigawatt) with 1 GW equivalent to  $1.4 \times 10^6$  kg H<sub>2</sub>O hr<sup>-1</sup> in integrated precipitation.  
678 Clusters are calculated from the TRMM-3B42 precipitation product, over the Tropics, May-  
679 September 1998-2008. The least squares best-fit exponent before the cutoff (fit over the scale-free  
680 range up to  $10^5$  GW for the 0.7 mm hr<sup>-1</sup> threshold) is -1.50.

681 Fig. 2 Examples of precipitation clusters from selected TRMM-3B42 time slice for rain rate  
682 thresholds 0.1 mm hr<sup>-1</sup> and 0.7 mm hr<sup>-1</sup>, as indicated. The spatial distribution of each cluster is  
683 shown with the power integrated over the cluster given by the legend.

684 Fig. 3 Same as Fig. 1, but for GFDL-HIRAM AMIP simulations at two resolutions (C180 and  
685 C360). For readability, HIRAM-C180 AMIP distributions have been shifted up vertically by a  
686 decade. The least squares best-fit exponent before the cutoff is -1.36 for HIRAM C180 and -1.39  
687 for HIRAM-C360.

688 Fig.4 Same as in Fig. 3, but comparing modeled cluster power probability distributions between  
689 resolutions for the 0.7 mm hr<sup>-1</sup> rain rate threshold, with no vertical shift of the HIRAM C180  
690 distribution. Note that the normalization differs simply because the course resolution model does  
691 not extend to as small a minimum cluster size.

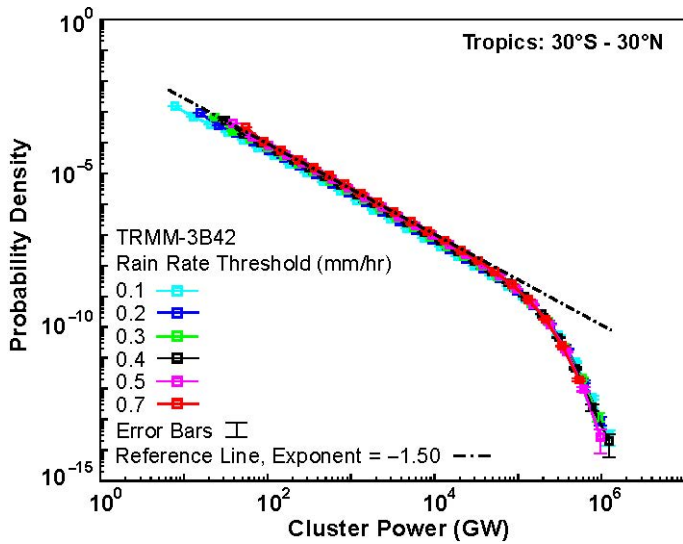
692 Fig. 5 Observed (TRMM-3B42) and modeled (HIRAM-C360 AMIP) Tropics cluster power  
693 probability distributions for May-September 1998-2008 for rain rate thresholds 0.3 mm hr<sup>-1</sup> and  
694 0.7 mm hr<sup>-1</sup>. Also plotted are cluster probability distributions at each rain rate threshold from a

695 synthetic time series created by random selections from 1979-1999 HIRAM-C360 AMIP data  
696 that preserve probability distributions at each point but not spatial correlations (see text). The  
697 distributions for the  $0.7 \text{ mm hr}^{-1}$  rain rate threshold have been shifted up vertically by two decades  
698 to improve readability.

699 Fig. 6 Same as Fig. 3, displaying a comparison of HIRAM cluster power probability distributions  
700 at two resolutions for historical (AMIP, May-September 1998-2008) and future (SST2030/2090,  
701 May-September 2026-2035/2086-2095) simulations for the  $0.7 \text{ mm hr}^{-1}$  rain rate threshold.  
702 HIRAM-C180 cluster power distributions have been shifted up vertically by a decade for  
703 readability.

704 Fig. 7 (a) As in Fig. 6, the change in the distribution of cluster power between historical (AMIP)  
705 and future (SST2090) simulations for the  $0.7 \text{ mm hr}^{-1}$  rain rate threshold using the higher  
706 resolution HIRAM (C360), with probability increase factors displayed for selected bins above the  
707 cutoff (vertical arrows). Horizontal arrow shows the estimated power increase for the probability  
708 value at the highest bin that can be estimated in current climate. (b) The change in cluster power  
709 distribution displayed as a risk ratio of the probability density for end-of-century to that in the  
710 historical period. Magenta line shows the risk ratio as estimated from the curves in (a); black and  
711 gray curves show tests of sensitivity to alternate bin-width choices: asymptotic bin widths of  
712  $0.1920$  (black),  $0.1960$  (cyan). (c) Black and magenta curves same as Fig. 7a, with an additional  
713 comparison (red) to the AMIP dataset with a CC-scaling factor applied (see text).

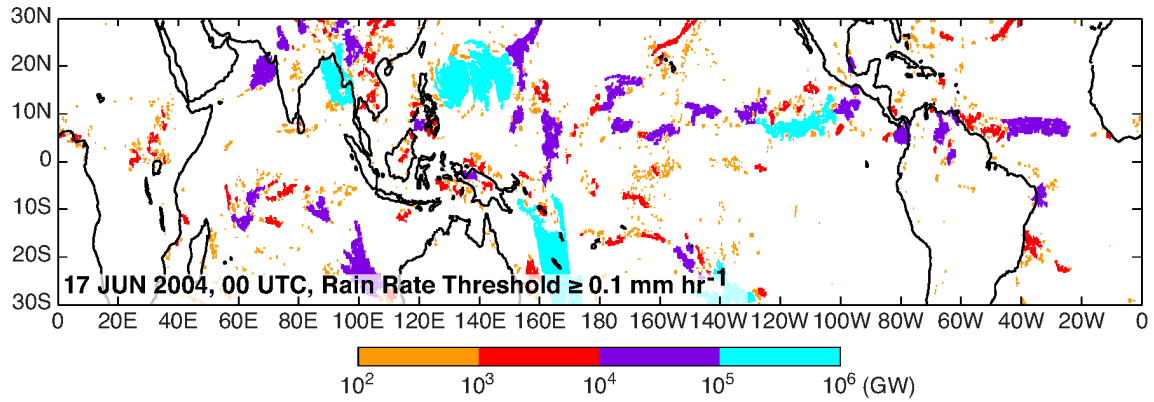
714



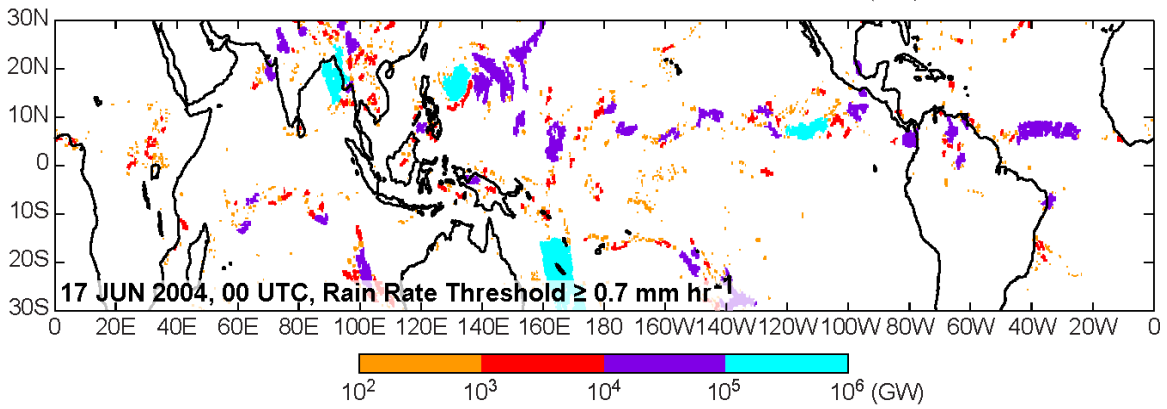
715

716 Fig. 1 Probability distributions of cluster power, i.e., precipitation integrated over clusters of  
 717 contiguous pixels exceeding the specified rain rate threshold, expressed in units of latent heat  
 718 release (gigawatt) with 1 GW equivalent to  $1.4 \times 10^6$  kg  $\text{H}_2\text{O}$   $\text{hr}^{-1}$  in integrated precipitation.  
 719 Clusters are calculated from the TRMM-3B42 precipitation product, over the Tropics, May-  
 720 September 1998-2008. The least squares best-fit exponent before the cutoff (fit over the scale-free  
 721 range up to  $10^5$  GW for the 0.7 mm  $\text{hr}^{-1}$  threshold) is -1.50.

722



723

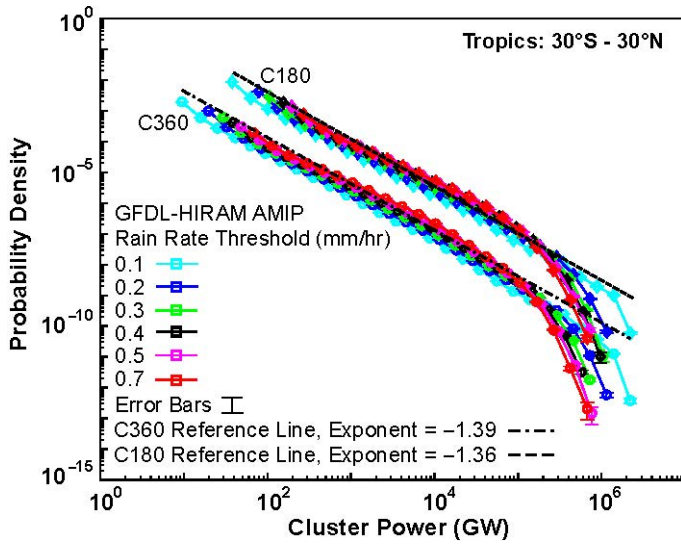


724

725 Fig. 2 Examples of precipitation clusters from selected TRMM-3B42 time slice for rain rate  
726 thresholds  $0.1 \text{ mm hr}^{-1}$  and  $0.7 \text{ mm hr}^{-1}$ , as indicated. The spatial distribution of each cluster is  
727 shown with the power integrated over the cluster given by the legend.

728

728



729

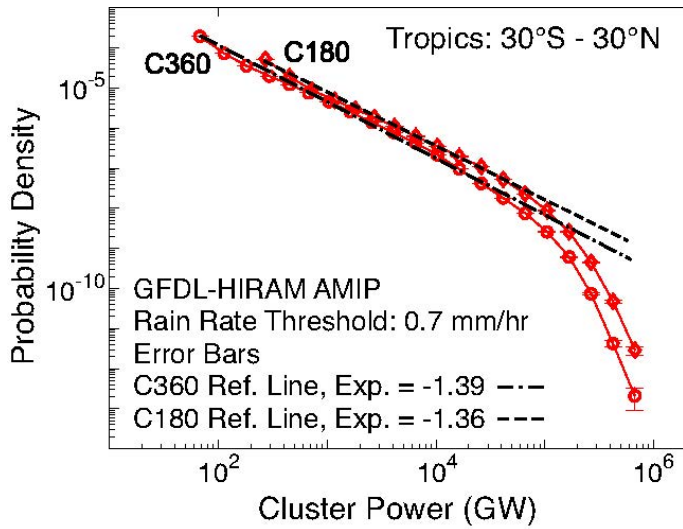
730 Fig. 3 Same as Fig. 1, but for GFDL-HIRAM AMIP simulations at two resolutions (C180 and  
731 C360). For readability, HIRAM-C180 AMIP distributions have been shifted up vertically by a  
732 decade (i.e. its y-axis values are offset by 1 power of 10). The least squares best-fit exponent  
733 before the cutoff is -1.36 for HIRAM C180 and -1.39 for HIRAM-C360.

734

735

736

737



738

739 Fig.4 Same as in Fig. 3, but comparing modeled cluster power probability distributions between  
 740 resolutions for the 0.7 mm hr<sup>-1</sup> rain rate threshold , with no vertical shift of the HIRAM C180  
 741 distribution. Note that the normalization differs simply because the course resolution model does  
 742 not extend to as small a minimum cluster size.

743

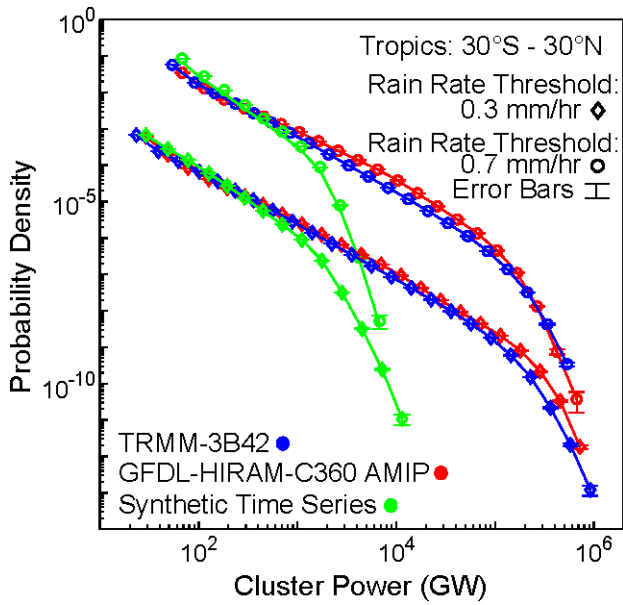
744

745

746

747

748

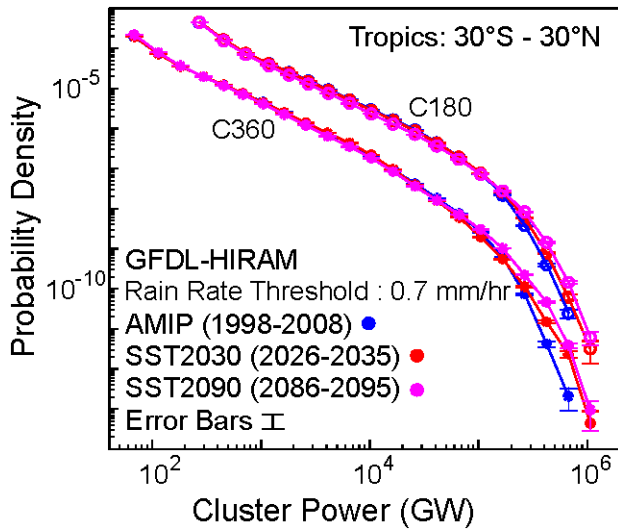


749

750 Fig. 5 Observed (TRMM-3B42) and modeled (HIRAM-C360 AMIP) Tropics cluster power  
 751 probability distributions for May-September 1998-2008 for rain rate thresholds  $0.3 \text{ mm hr}^{-1}$  and  
 752  $0.7 \text{ mm hr}^{-1}$ . Also plotted are cluster probability distributions at each rain rate threshold from a  
 753 synthetic time series created by random selections from 1979-1999 HIRAM-C360 AMIP data  
 754 that preserve probability distributions at each point but not spatial correlations (see text). The  
 755 distributions for the  $0.7 \text{ mm hr}^{-1}$  rain rate threshold have been shifted up vertically by two decades  
 756 to improve readability.

757

758



759

760 Fig. 6 Same as Fig. 3, displaying a comparison of HIRAM cluster power probability distributions  
 761 at two resolutions for historical (AMIP, May-September 1998-2008) and future (SST2030/2090,  
 762 May-September 2026-2035/2086-2095) simulations for the 0.7 mm hr<sup>-1</sup> rain rate threshold.

763 HIRAM-C180 cluster power distributions have been shifted up vertically by a decade for  
 764 readability.

765

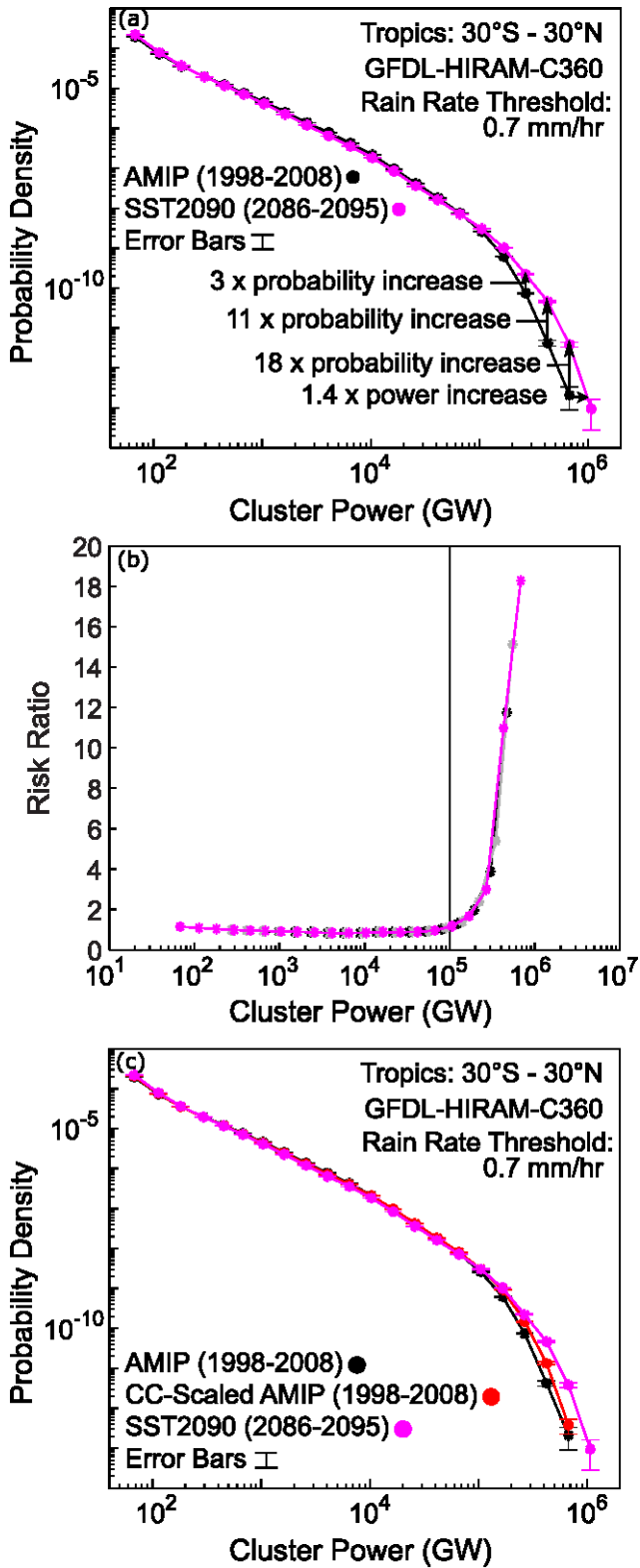
766

767

768

769

770



771

772 Fig. 7 (a) As in Fig. 6, the change in the distribution of cluster power between historical (AMIP)

773 and future (SST2090) simulations for the  $0.7 \text{ mm hr}^{-1}$  rain rate threshold using the higher

774 resolution HIRAM (C360), with probability increase factors displayed for selected bins above the  
775 cutoff (vertical arrows). Horizontal arrow shows the estimated power increase for the probability  
776 value at the highest bin that can be estimated in current climate. (b) The change in cluster power  
777 distribution displayed as a risk ratio of the probability density for end-of-century to that in the  
778 historical period. Magenta line shows the risk ratio as estimated from the curves in (a); black and  
779 gray curves show tests of sensitivity to alternate bin-width choices: asymptotic bin widths of  
780 0.1920 (black), 0.1960 (cyan). (c) Black and magenta curves same as Fig. 7a, with an additional  
781 comparison (red) to the AMIP dataset with a CC-scaling factor applied (see text).

782

783

784